Chapter 3

Solar PV Integration of the Electrolytic Capacitor-less Isolated DC-DC Resonant Converter

3.1 Introduction

The previous chapter discusses the design and operation of the two electrolytic capacitor-less isolated DC-DC resonant converters. In this chapter, the earlier discussed resonant converters DHABRC is integrated with solar PV. In Solar PV integrations, a single-peak PV curve is observed when the solar irradiance is uniform; however, when the solar irradiance is non-uniform or shaded, a multi-peak PV curve is observed. Conventional maximum power point tracking (MPPT) algorithms like perturb and observe (P&O) and incremental conductance (INC) are only suitable for tracking solar power observed under uniform irradiance conditions. An advanced version of the conventional or optimization-based MPPT algorithm is required to track the multi-peak PV characteristic observed under non-uniform irradiance conditions. The partial shaded or non-uniform irradiance conditions are observed when the solar panels are shaded from foreign objects like buildings, birds, clouds, etc. A Chroma's Solar PV emulator is utilized to emulate different shaded PV curves of different voltage and current ratings for solar PV integration.

3.2 Solar PV Integration of Dual Half Active Bridge Resonant Converter

The proposed dual half-active bridge resonant converter is integrated with Solar PV using a solar PV emulator (Chroma 62100H-600S). The circuit diagram of the solar PV integrated proposed converter is shown in Fig. 3.1. For tracking the solar power, metaheuristic optimization-based maximum power point tracking algorithms, i.e., Particle Swarm Optimization and Grey Wolf Optimization, are utilized, which is discussed later in the chapter. For harnessing solar energy, a voltage sensor (LV 25-P) and a current sensor (LA 25-P) are utilized and connected to the input of the proposed converter. The voltage sensor senses the input PV voltage (V_{in}), and the current sensor senses the input PV current (I_{in}), as shown in Fig. 3.1. The sensed PV voltage and current are sent as an input to the ADC pins of the Texas Instruments microcontroller TMS320F28335 for analog to digital conversion. The MPPT algorithm is executed using the sensed data until it converges to achieve the global peak power point. Since the proposed converters are phase-shift modulated (control parameter) converters, the algorithm's output will be a phase-shift angle. This phase-shift angle will be further utilized to generate the gating signals for the secondary side active switches (S_3 and S_4).

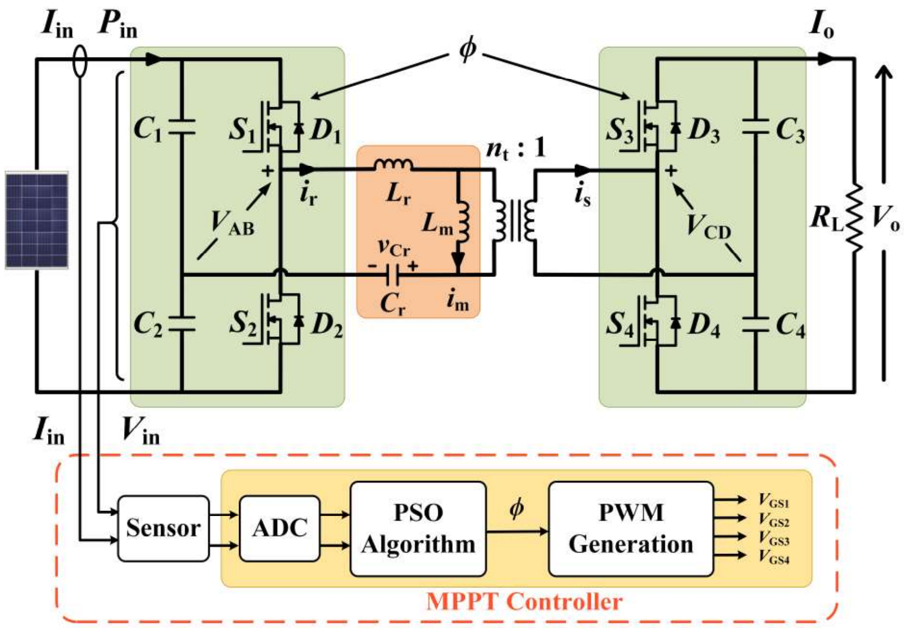

Fig. 3.1 Circuit diagram of the solar panel integrated DHABRC.

3.3 Particle Swarm Optimization

The proposed converter is integrated with a PV source that is operated at MPP with the help of a particle swarm optimization (PSO) based MPPT algorithm. PSO is a metaheuristic evolutionary computational technique inspired by the natural phenomenon of swarm foraging. In PSO, each particle i (i=1 to swarm size 'n') is a candidate solution, and it can be represented as a position vector $x_i = [x_{i1}, x_{i2} \ldots x_{id}]$ and velocity vector $v_i = [v_{i1}, v_{i2} \ldots v_{id}]$ in d-dimension of search space. Social interaction is the key feature of PSO, where each particle of the swarm learns from the others. Using the ability of exploration and exploitation, the swarm flies through space in search of the best fitness value while modifying their velocity and position towards personal best P_{bi} and global best G_b given as:

$$v_i^{k+1} = wv_i^k + c_1 r_1 (P_{bi}^k - x_i^k) + c_2 r_2 (G_b^k - x_i^k) \quad (3.1)$$

$$x_i^{k+1} = x_i^k + v_i^{k+1} \quad (3.2)$$

Since the proposed converter is a phase-shift modulated converter, so for PSO, n = 3 (solution particles) phase-shift angles (ϕ) are optimally chosen (for the given voltage and power rating of the design) and used as the initial particle position for the MPPT operation. So, (3.1) and (3.2) will be revised as (3.3) and (3.4).

$$v_i^{k+1} = wv_i^k + c_1 r_1 (P_{bi}^k - \phi_i^k) + c_2 r_2 (G_b^k - \phi_i^k) \tag{3.3}$$

$$\phi_i^{k+1} = \phi_i^k + v_i^{k+1} \tag{3.4}$$

where k is the number of iterations, w is the inertia coefficient of the particle, c_1 - c_2 is the constants of the cognitive and social weighting factor and r_1 - r_2 is the random number that varies between 0 and 1. The movement of the particles involves its self-momentum, cognitive, and social parts, as shown in Fig. 3.2. The flowchart for the algorithm is given in Fig. 3.3.

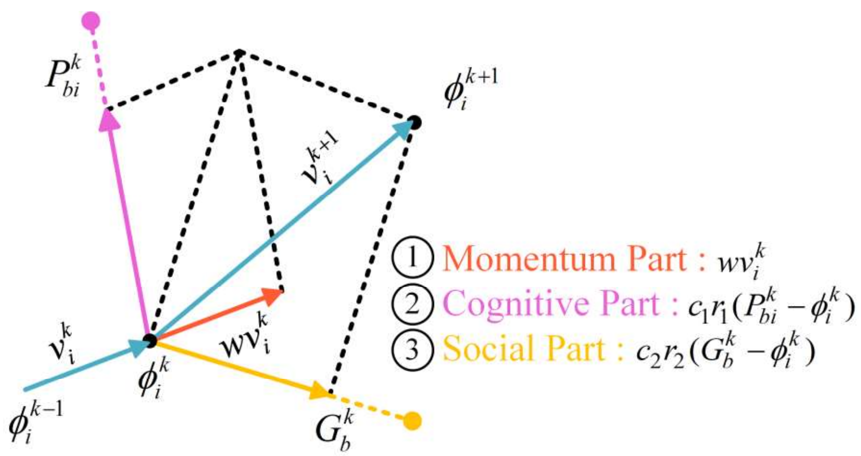

Fig. 3.2 Movement of solution particle of the PSO in search space.

The phase-shift angle produced from the algorithm is used to produce the gate pulses for the switches, as shown in Fig. 3.4. The gate pulses V_{GS2} and V_{GS4} of switches S_2 and S_4 are complements of gate pulse V_{GS1} and V_{GS3}, respectively. For the proposed converter, the power is controlled by the phase-shift angle. So, the phase-shift angle will be included as the position vector $x_i{}^k$. The parameter $v_i{}^k$ is the velocity vector, representing the change in the position vector or phase-shift angle. The maximum power point tracking requires a continuous change in phase-shift angle to maximize the input PV power, which is the ultimate goal of harnessing the power efficiently. For this, the small values of velocity vectors are chosen to control the variation in the phase-shift angle. The operation of the PSO algorithm can be explained in the following steps:

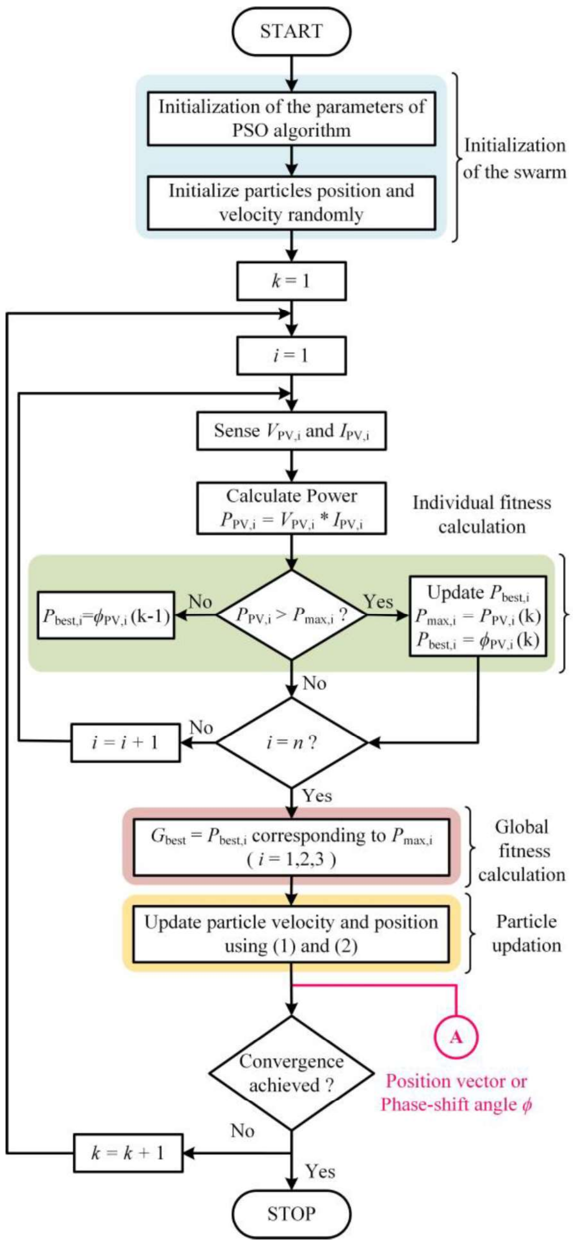

Fig. 3.3 Flowchart of the PSO algorithm.

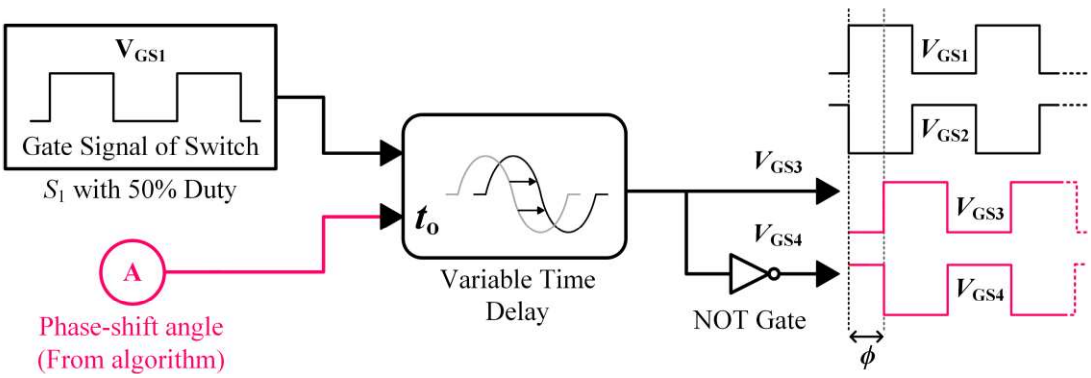

Fig. 3.4 Pulse generation using phase-shift angle obtained from the algorithm.

Step 1: In the PSO algorithm, n number of phase-shift angles are chosen and used as the initial particle position.

Step 2: The converter is operated with the initially chosen phase-shift angles, and the power corresponding to these phase-shift angles is compared with their past values. The power is changed if the following condition is satisfied:

$$f(x_i^k) > f(P_{bi}^k) \tag{3.5}$$

Then $f(P_{bi}^k) = f(x_i^k)$ and $P_{bi} = x_i$. Here f denotes the objective function or PV power input.

Step 3: Now, the performance of the personal best is compared with the global best using the conditions:

$$f(P_{bi}^k) > f(G_b^k) \tag{3.6}$$

If (3.6) satisfies, then $f(G_b^k) = f(P_{bi}^k)$ and $G_b^k = P_{bi}^k$.

Step 4: Now, update the particle's velocity and position using (3.3) and (3.4).

Step 5: Repeat the steps till the algorithm is converged.

The algorithm offers many advantages, such as the capability to track global peak power under PSC, adaptability to dynamic conditions, fewer oscillations, less sensitivity to noise, less mathematical complexities, and a direct control approach, causing the elimination of the control loops.

Table 3.1 Design parameters of the solar PV integrated DHABRC and PSO

Parameters	Value	Parameters	Value
Input Voltage V_{in}	140 V	Particles	3
Output Voltage V_o	125-115	w	0.4
Output Power P_o	500 W	c_1	1.45
Switching Frequency F_s	50 kHz	c_2	1.63
Resonant Inductor L_r	60.68 μH	r_1 and r_2	(0,1)
Parallel Inductor L_m	292 μH	n_t	28:25
Resonant Capacitor C_r	240.43 nF	C_1 - C_4	20 μF

Table 3.2 Parameters of the shading patterns for PSCs for simulation results

Shading Patterns	Global Peak (GP)		Open Circuit Voltage V_{oc}	Local Peak (LP)		Tracking Time (sec.)	Tracking Efficiency (%)
	Peak Power	Peak Voltage		Power	Voltage		
SP-1	482.5	168.5	206.6	461.9	123.8	0.165	99.52
SP-2	439.9	131.8	207.2	391.1	181.4	0.195	99.44

3.4 Simulation Results for PSCs using PSO

The design parameters of the converter DHABRC are shown in Table 3.1, and the parameters of the two shading patterns are shown in Table 3.2. The shading pattern-1 (SP-1) has a global peak (GP) power of 482.5 watts at 168.5 volts, as shown in Fig. 3.5 (a). The local peak (LP) can be observed at 461.9 watts at 123.8 volts. SP-2 is a two-peak PV curve with a global peak (GP) at 439.9 watts with a voltage of 131.8 and a local peak (LP) at 391.1 watts with 181.4 volts, as shown in Fig. 3.5 (b). Fig. 3.5 (c)-(h) shows the simulation results for the above two shading patterns. For SP-1, the phase shift angle (ϕ), input power (P_{PV}), and input voltage V_{in} have been shown in Fig. 3.5 (c). In Fig. 3.5 (d), the primary bridge voltage (V_{AB}) and corresponding bridge current (i_r) have been shown. In Fig. 3.5 (e), the secondary bridge voltage (V_{CD}) and corresponding bridge current (i_s) have been shown. The algorithm takes approximately 0.165 seconds to track the global peak power.

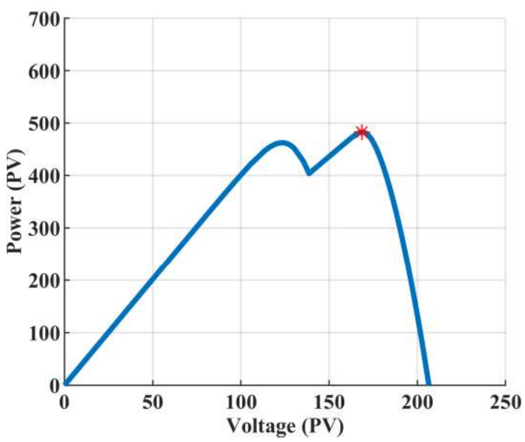

(a)

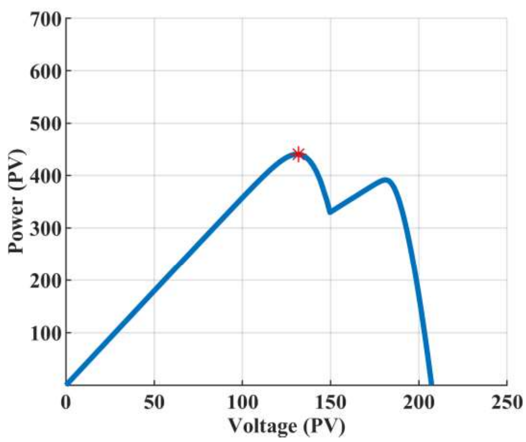

(b)

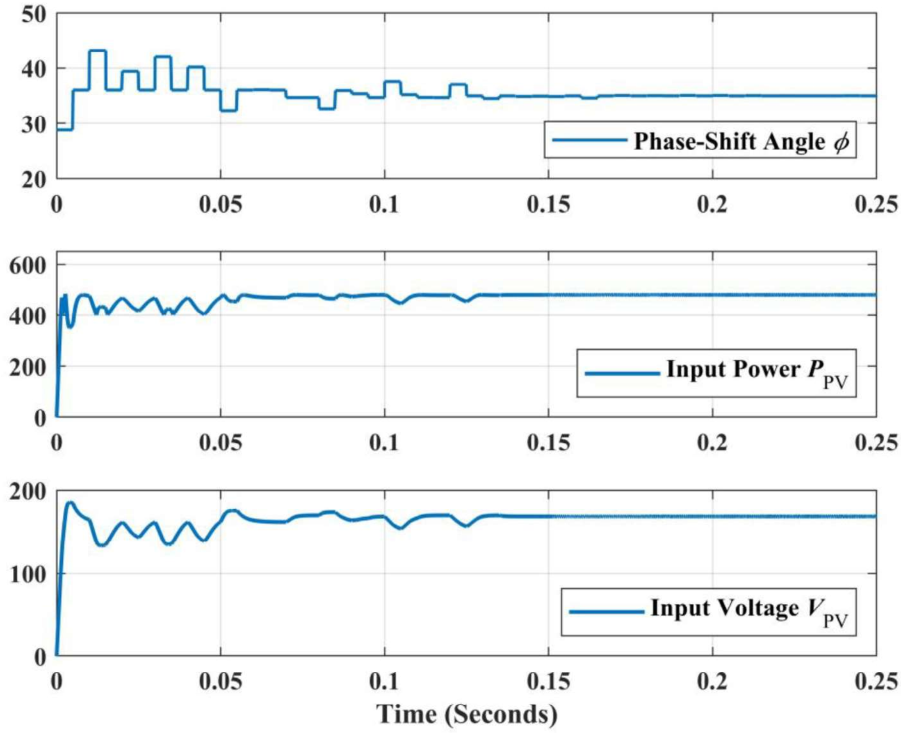
Phase-Shift Angle ϕ
Input Power P_{PV}
Input Voltage V_{PV}
Time (Seconds)

(c)

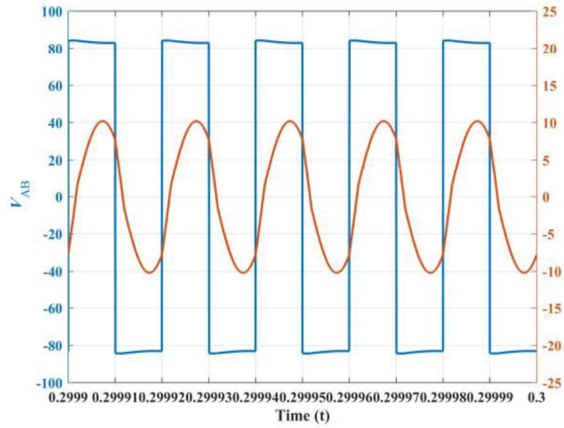
V_{AB}
i_r
Time (t)

(d)

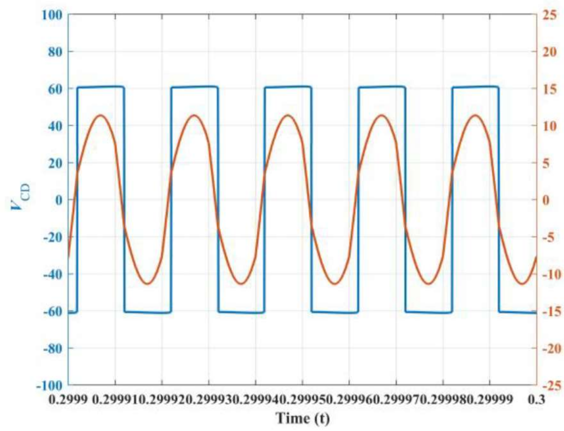
V_{CD}
i_s
Time (t)

(e)

For SP-2, the phase shift angle (ϕ), input power (P_{PV}), and input voltage V_{in} have been shown in Fig. 3.5 (f). In Fig. 3.5 (g), the primary bridge voltage (V_{AB}) and corresponding bridge current (i_r) have been shown. In Fig. 3.5 (h), the secondary bridge voltage (V_{CD}) and corresponding bridge current (i_s) have been shown. The algorithm takes approximately 0.195 seconds to track the global peak power. From Fig. 3.5 (c)–(f), it can be seen that the PSO-based MPPT algorithm works satisfactorily for the given input voltage range, and the steady-state voltages are oscillation-free.

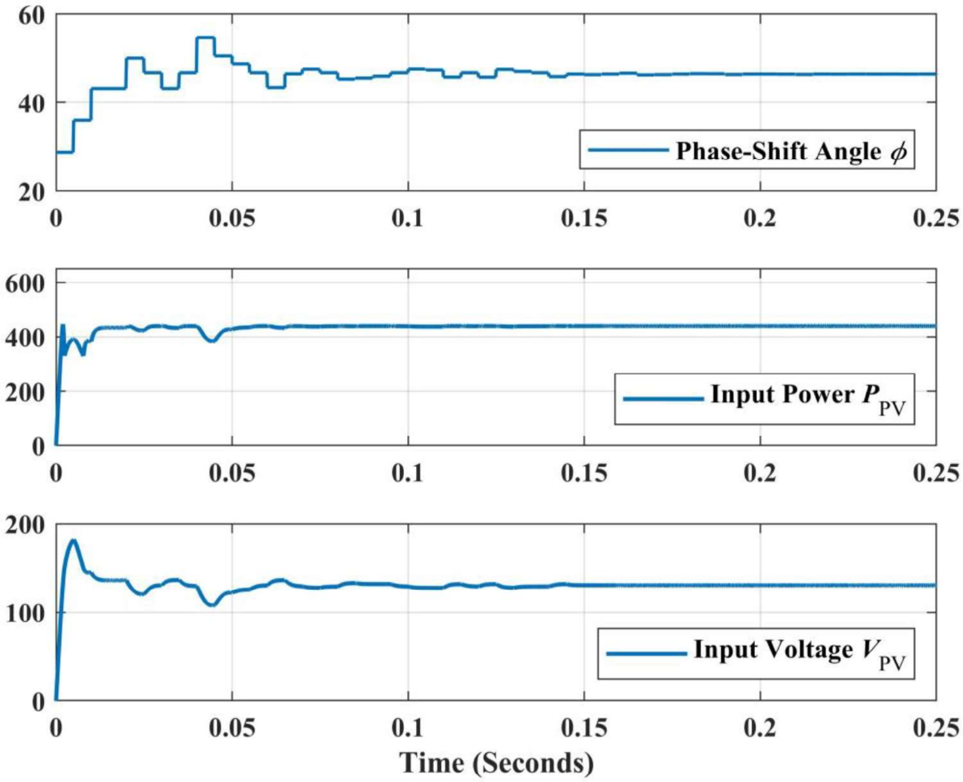

(f)

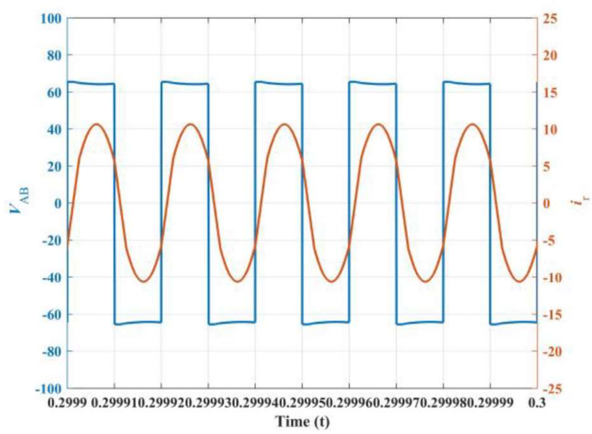

(g)

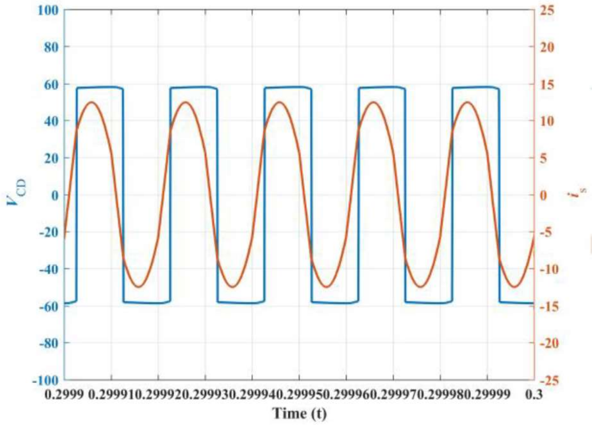

(h)

Fig. 3.5 Simulation results for PSO showing shading pattern (a) SP-1 (b) SP-2 (c)-(h) Simulation results showing phase shift angle (ϕ), input power (P_{PV}), input voltage V_{in}, bridge voltages (V_{AB} and V_{CD}) and corresponding bridge currents (i_r and i_s).

Table 3.3 Parameters of the shading patterns for PSCs and experimental results

Shading Patterns	**Global Peak (GP)**		V_{oc}	**Local Peak (LP)**		**Tracking Time (sec.)**	**Tracking Efficiency (%)**
	Peak Power	**Peak Voltage**		**Power**	**Voltage**		
SP-1	452.5	153.6	209.8	405.97	116.58	1.20	99.68
				420.28	179.23		
SP-2	480.4	162.8	213.1	477.8	138.6	1.08	99.82
SP-3	451.1	144.3	213.1	449.2	127.017	1.12	99.7
				446.2	163		
SP-4	369.9	129.4	208.1	366	157.3	1.16	99.8

3.5 Experimental Results for PSCs using PSO

Partial shading conditions (PSC) are one of the most practical challenges in solar PV operation, leading to multi-peak PV characteristics. The PSCs are tested using four shading patterns (SP) of different power and voltage ratings. The input voltage and current are sensed at a time interval of 0.04 s to keep the waveform noise-free from the designed circuit board. Three solution particles (phase-shift angles $\phi_1 = 30$, $\phi_2 = 35$, and $\phi_3 = 40$) are selected to cover a vast search space and operated with a sampling time (MPPT) of 0.04 s. The PSO time step (or time consumption of one iteration with three solution particles) is 0.12 seconds. The shading patterns SP-1 to SP-4 and their corresponding MPP tracking results are shown in Fig. 3.6 (a)-(h). The parameters of these shading patterns, their tracking time, and their MPP tracking efficiency observed from hardware testing are given in Table 3.3. For different shading conditions, the algorithm takes approximately 8-10 iterations (1-1.2 seconds) to track the global peak successfully. The tracking efficiency for all the shading patterns is more than 99.6%.

The shading pattern-1 (SP-1) has three peaks with a global peak (GP) power of 452.5 watts at 153.6 volts, as shown in Fig. 3.6 (a). The other two local peaks (LP) can be observed at 405.97 watts with 116.58 volts and 420.28 watts with 179.23 volts. The algorithm takes approximately 1.2 seconds to track the global peak power.

SP-2 also has a two-peak PV curve, as shown in Fig. 3.6 (b). The global peak (GP) can be observed at 480.4 watts with a voltage of 162.8. The local peak (LP) can be observed at 477.8 watts with 138.6 volts. The algorithm takes 1.08 seconds to track the global peak.

SP-3 is a three-peak PV curve, as shown in Fig. 3.6 (c). The global peak (GP) power for the SP-3 can be observed at 451.1 watts with 144.3 volts. The other two local peaks (LP) are at 449.2 watts with 127.017 volts and 446.2 watts with 163 volts. The PSO-based maximum power point tracking algorithm takes approximately 1.12 seconds to track the global peak power.

SP-4 is a two-peak PV curve, as shown in Fig. 3.6 (d). The global peak (GP) can be observed at 369.9 watts with 129.4 volts. The local peak (LP) can be observed at 366 watts with 157.3 volts. From Fig. 3.6 (a)–(h), it can be seen that the PSO-based MPPT algorithm works satisfactorily for the given input voltage range, and the steady-state voltages are oscillation-free.

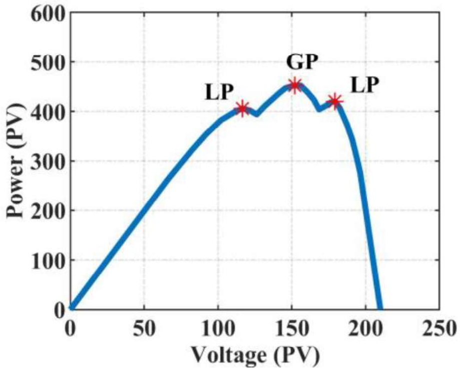
Power (PV)
Voltage (PV)
0
100
200
300
400
500
600
0
50
100
150
200
250
LP
GP
LP

(a)

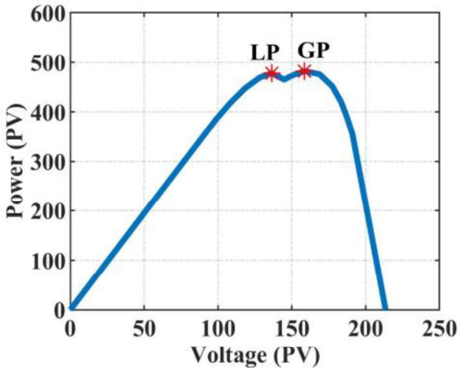
Power (PV)
Voltage (PV)
0
100
200
300
400
500
600
0
50
100
150
200
250
LP
GP

(b)

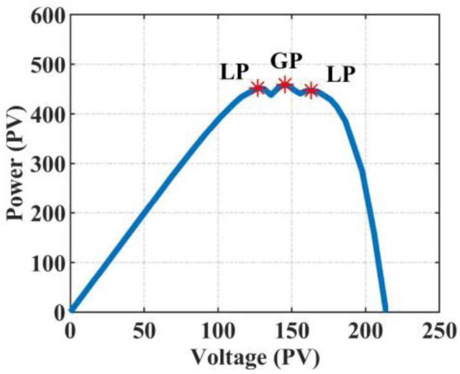
Power (PV)
Voltage (PV)
0
100
200
300
400
500
600
0
50
100
150
200
250
LP
GP
LP

(c)

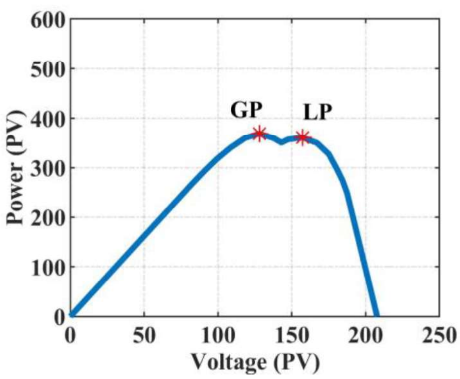
Power (PV)
Voltage (PV)
0
100
200
300
400
500
600
0
50
100
150
200
250
GP
LP

(d)

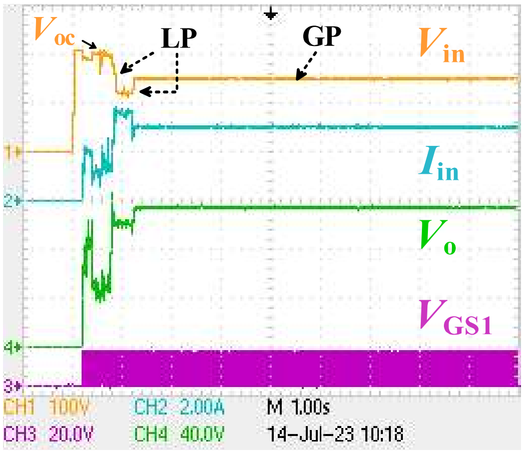

Voc
LP
GP
Vin
Iin
Vo
VGS1
CH1 100V
CH2 2.00A
M 1.00s
CH3 20.0V
CH4 40.0V
14-Jul-23 10:18

(e)

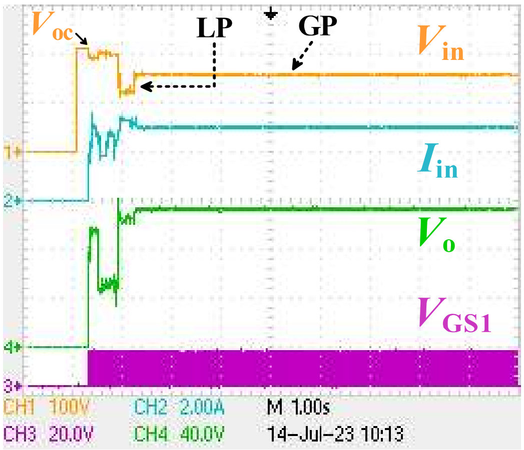

Voc
LP
GP
Vin
Iin
Vo
VGS1
CH1 100V
CH2 2.00A
M 1.00s
CH3 20.0V
CH4 40.0V
14-Jul-23 10:13

(f)

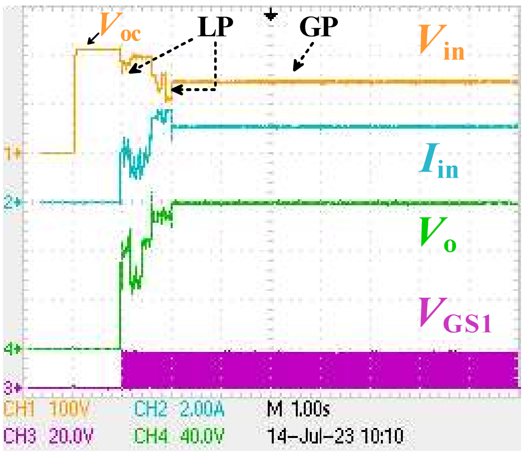

Voc
LP
GP
Vin
Iin
Vo
VGS1
CH1 100V
CH2 2.00A
M 1.00s
CH3 20.0V
CH4 40.0V
14-Jul-23 10:10

(g)

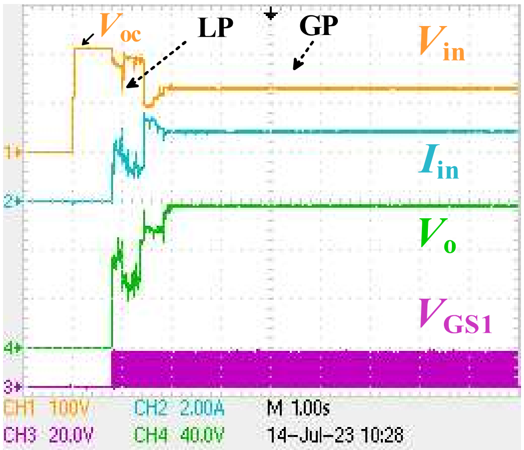

(h)

Fig. 3.6 Experimental results for PSO showing shading patterns with local peak (LP) and global peak power (GP) (a) SP-1 (b) SP-2 (c) SP-3 (d) SP-4 and their (e)-(h) Hardware results showing input voltage V_{in} and current I_{in}, output voltage V_o, and gate signal V_{GS1}.

3.6 Grey Wolf Optimization (GWO)

For solar PV to converter integration, a conventional grey wolf optimization-based maximum power point tracking (MPPT) algorithm is utilized to harness the maximum power under uniform irradiance and partial shading conditions. The GWO is one of the bio-inspired, metaheuristic optimization algorithms developed by Mirjalili et al. in 2014. The algorithm imitates the social hierarchy and hunting behavior of the apex predators' grey wolves. Based on the dominating behavior, the social hierarchy of the grey wolf is shown in Fig. 3.7. The alpha wolves (α_g) are the leaders responsible for making decisions. The beta wolves (β_g) help the alpha in decision-making and implementing the decisions among the pack. Omega wolves (ω_g), the weakest members of the pack, are dominated by delta wolves (δ_g), who serve as the elders, scouts, and caretakers. For MPPT operation, the same hierarchy is used for problem-solving, whereas alpha wolve is considered the best solution. The hunting mechanism of the wolves has three main parts: chasing/tracking, encircling, and hunting the prey. The vector representation of the encircling behavior of the wolves in terms of distance vector 'D' can be given as follows.

$$\vec{D} = |\vec{C_g} \cdot \vec{X}_p(k) - \vec{X}(k)| \tag{3.7}$$

$$\vec{X}(k+1) = \vec{X}_p(k) - \vec{A} \cdot \vec{D} \tag{3.8}$$

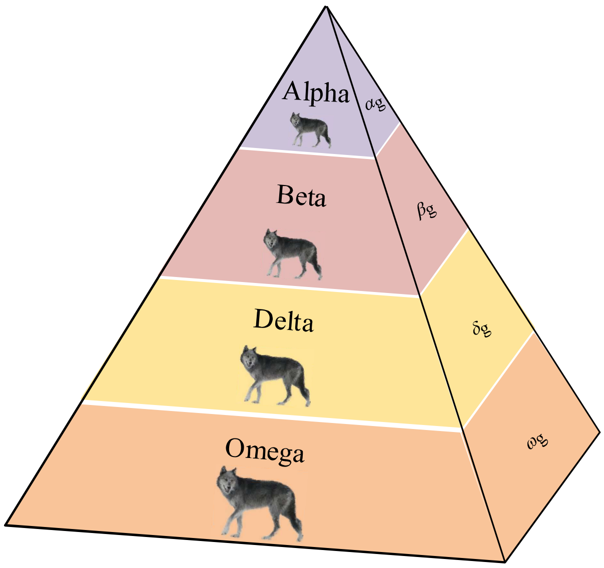

Fig. 3.7 Social hierarchy of the grey wolves based on their dominance/solution in the pack.

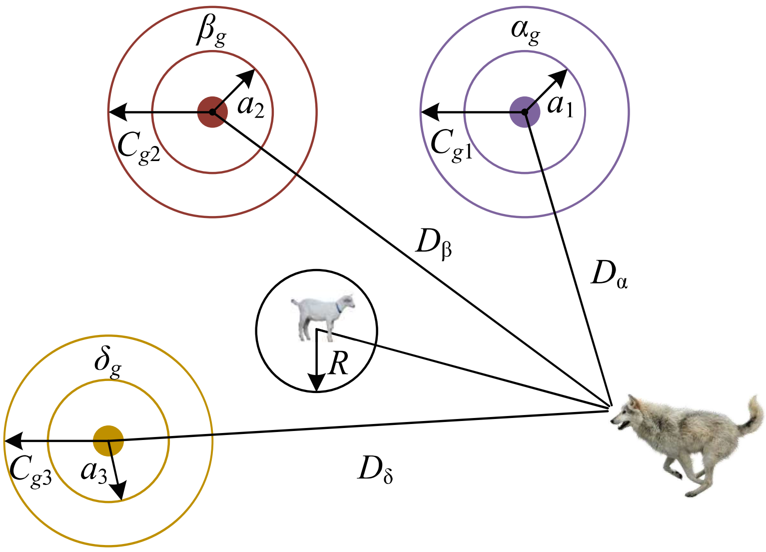

Fig. 3.8 Movement of the grey wolves for hunting.

Here, 'X_p' and 'X' represent the position vector for the prey and the wolves, k is the number of iterations, and coefficient vectors 'A' and 'C_g' can be given as (3.9) and (3.10).

$$\vec{A} = 2\vec{a} \cdot \vec{r}_1 - \vec{a} \tag{3.9}$$

$$\vec{C}_g = 2 \cdot \vec{r}_2 \tag{3.10}$$

Here, vector 'a' decreases linearly from 2 to 0, r_1 and r_2 are the random vectors that vary between (0,1). Based on the mathematical model, the movement of the grey wolves for hunting is shown in Fig. 3.8. For the proposed converter, the controlling parameter is the phase-shift angle, which will be used as the wolves' position. So, (3.8) can be rewritten as (3.11).

$$\vec{\phi}(k+1) = \vec{\phi}(k) - \vec{A} \cdot \vec{D} \tag{3.11}$$

The positions of the wolves will be updated by taking the average of their positions calculated using (3.12).

$$\vec{\phi}(k+1) = \frac{\vec{\phi_1} + \vec{\phi_2} + \vec{\phi_3}}{3} \tag{3.12}$$

For solar PV integration, the panel voltage and current are sensed continuously and fed as input to the GWO algorithm. The GWO is a meta-heuristic algorithm that offers a direct control approach for generating phase-shift angles, eliminating the proportional-integral control loops. The switching signals are generated using the variable time delay based on the phase-shift angle. This angle is used to delay the gate signals of switch S_1 (V_{GS1}) to get the gate pulses for switch S_3 (V_{GS3}) and switch S_4 (V_{GS4}). The gate pulses of S_2 and S_4 are 180° phase shifted to the gate pulses of S_1 and S_3 respectively. Now, to harness the maximum power from solar panels, the phase-shift angle is continuously varied by the GWO algorithm till the PV panel voltage (input voltage) is settled to the value corresponding to the global peak power point, and the converter starts to harness the maximum power.

Table 3.4 Parameters of selected PV curves for UIC and PSC testing using GWO

PV Curve	**Global Power**		V_{oc}	**Local Power**		**Tracking Time (s)**
	P_{MP}	V_{MP}		**Power**	**Voltage**	
UIC-1	423.8	104.6	135.6	-	-	0.72
UIC-2	339.3	99.2	131.2	-	-	0.68
PSC-1	415.5	97.8	138	408.2	121.9	0.80
PSC-2	401	119.7	137	390.5	97.23	0.76
PSC-3	275.6	111.3	133.4	273.3	91.42	0.84
PSC-4	319.1	91.7	132.3	260.3	113.5	0.80

3.7 Experimental Results under GWO

The different tests conducted on DHABRC are as follows.

3.7.1 Results under Uniform Irradiance Conditions (UIC)

The performance of the proposed DHABRC is tested under two different uniform irradiance conditions (UICs) using a GWO-based MPPT algorithm. The parameters for these UICs are given in Table 3.4. The converter input voltage and current are sensed using LV 25-P and LA 25-P sensors and then provided as input to the microcontroller TMS320F28335 for executing the algorithm. The MPPT sensing time interval is 40 ms to avoid unnecessary noise sensed from the circuit board.

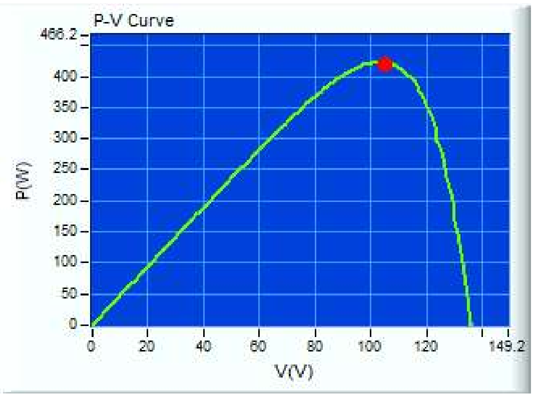

(a)

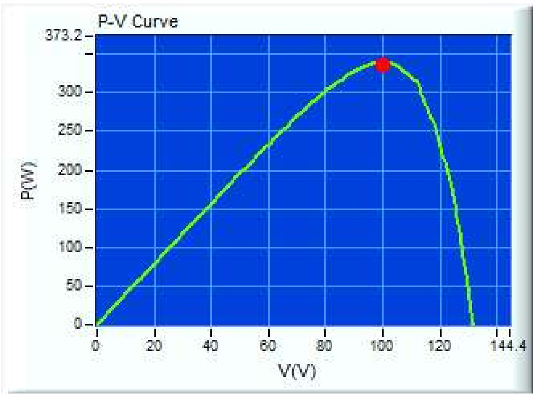

(b)

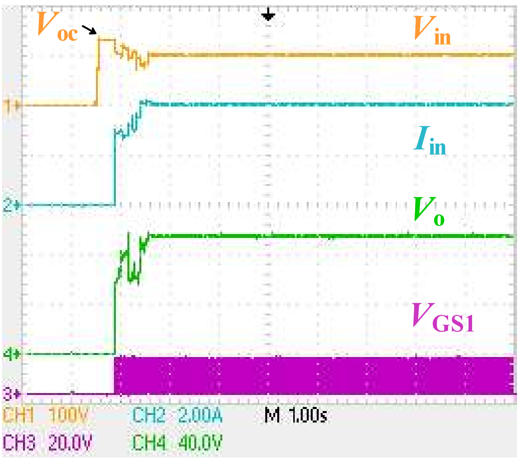

(c)

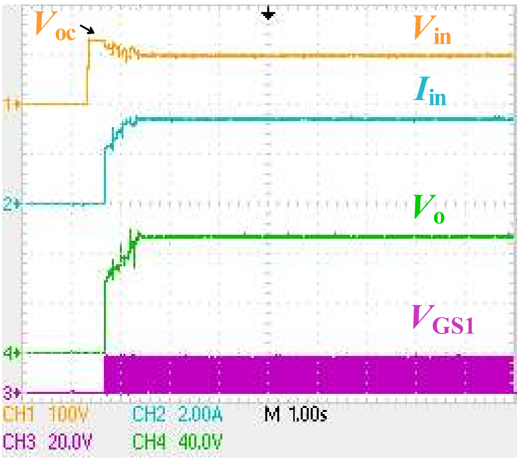

(d)

Fig. 3.9 Experimental results under uniform irradiance conditions (UIC) showing (a) UIC-1. (b) UIC-2 and corresponding experimental results show input voltage, input current, and output voltage with gate signal V_{GS1} in (c)-(d), respectively.

For UIC-1, the peak power and peak voltages are 423.8 W and 104.6 V, respectively, as shown in Fig. 3.9 (a). For UIC-2, the peak power and peak voltages are 339.3 W and 99.2 V, respectively, as shown in Fig. 3.9 (b). Upon execution of the algorithm, the input voltage quickly reaches the open-circuit voltage V_{OC} of the PV curve. For UIC-1, the PV curve and corresponding experimental results are shown in Fig. 3.9 (c). The peak power operation can be observed from the red dot on the PV curve. The peak power is successfully tracked within 6-7 iterations. The PV curve and the experimental results for the UIC-2 are shown in Fig. 3.9 (d). The algorithm takes 0.68 seconds to track the peak power for the UIC-2. It can be observed from the experimental results that the steady-state voltage and current waveforms are oscillation-free.

Also, the acceptable time to reach MPP after a change in irradiance is not a fixed time but depends upon various factors, such as type of algorithm, duty step, control parameters, and variation in irradiance or shading condition.

3.7.2 Results under Partial Shading Conditions (PSCs)

To test the performance of the proposed isolated DC-DC resonant converter under partial shading conditions (PSC), four different PV curves (PSC-1 to PSC-4) are created. The parameters for four PV curves are given in Table 3.4. For PSCs, three wolves with an initial value of phase-shift angles 30°, 35°, and 40° are chosen to cover a wide range of PV curves.

The partial shading condition-1 (PSC-1) has two peaks with a global peak (GP) power of 415.5 watts at 97.8 volts, as shown in Fig. 3.10 (a). The other local peak (LP) can be observed at 408.2 watts with 121.9 volts. PSC-2 is also a two-peak PV curve, as shown in Fig. 3.10 (b). The global peak (GP) can be observed at 401 watts with a voltage of 119.7. The other local peak (LP) can be observed at 390.5 watts with 97.23 volts.

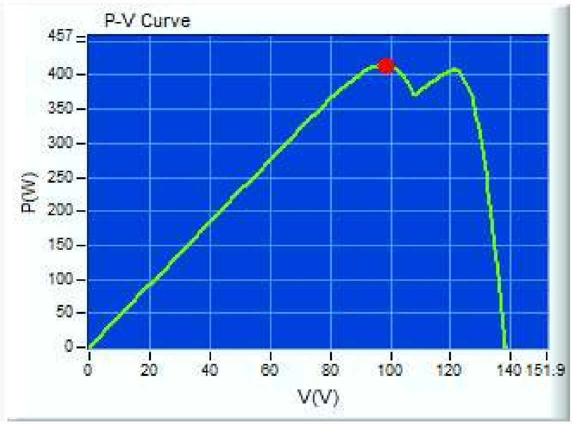

(a)

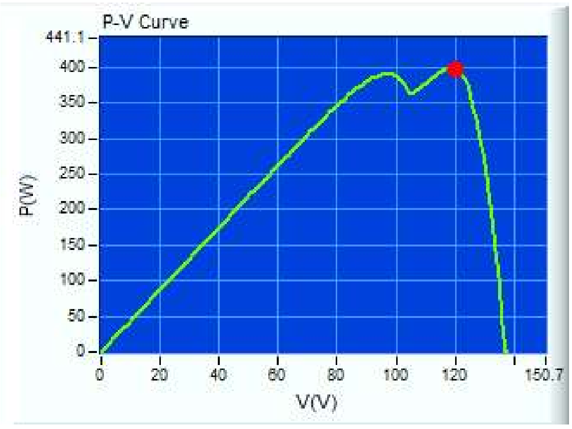

(b)

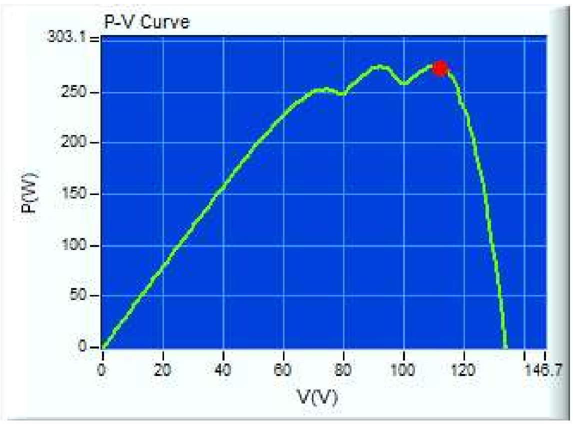

(c)

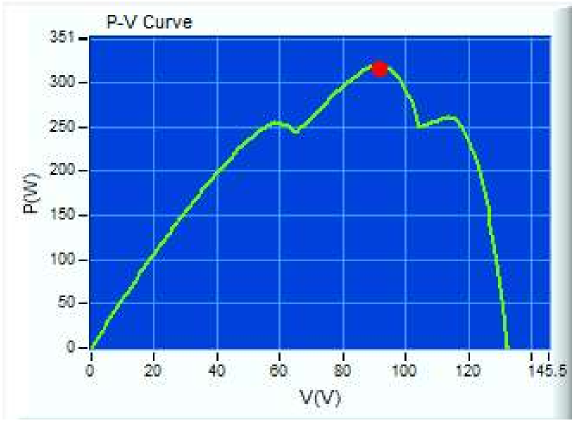
P-V Curve
P(W)
V(V)
351
300
250
200
150
100
50
0
0
20
40
60
80
100
120
145.5

(d)

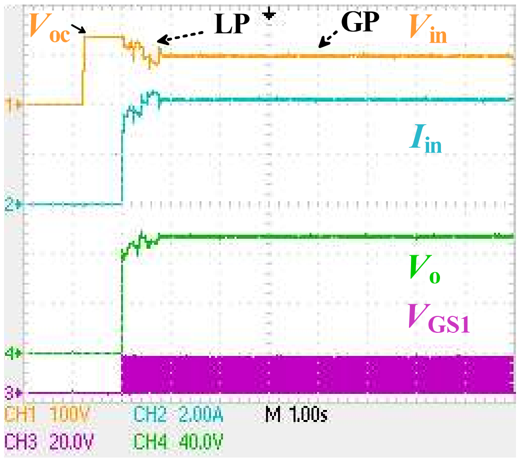
Voc
LP
GP
Vin
Iin
Vo
VGS1
CH1 100V
CH2 2.00A
M 1.00s
CH3 20.0V
CH4 40.0V

(e)

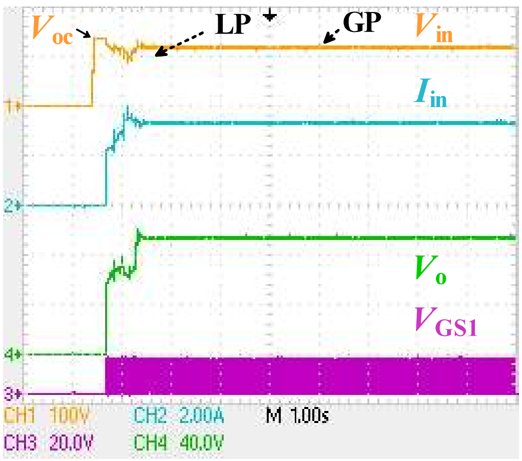
Voc
LP
GP
Vin
Iin
Vo
VGS1
CH1 100V
CH2 2.00A
M 1.00s
CH3 20.0V
CH4 40.0V

(f)

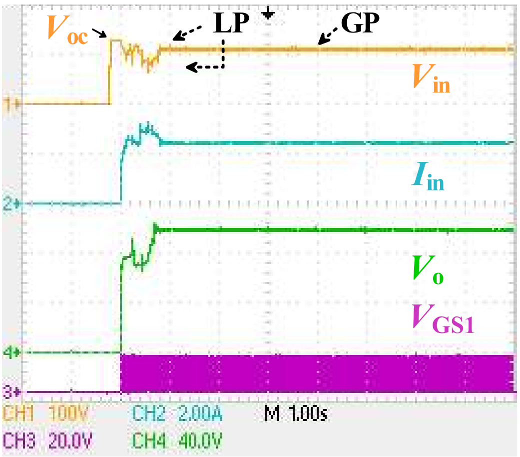

(g)

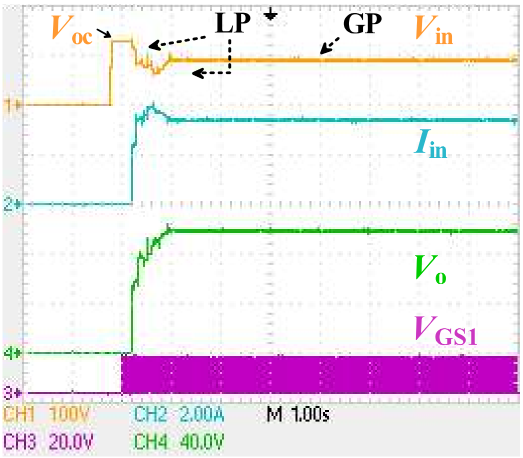

(h)

Fig. 3.10 Experimental results for PSCs showing their local peak (LP) and global power (GP) (a) PSC-1 (b) PSC-2 (c) PSC-3 (d) PSC-4 and their corresponding (e)-(h) Hardware results showing input voltage V_{in} and current I_{in}, output voltage V_o, and gate signal V_{GS1}.

PSC-3 is a three-peak PV curve, as shown in Fig. 3.10 (c). The global peak (GP) power for the PSC-3 can be observed at 275.6 watts with 111.3 volts. The other two local peaks (LP) are at 273.3 watts with 91.42 volts and 252.1 watts with 74.45 volts. PSC-4 is a three-peak PV curve, as shown in Fig. 3.10 (d). The global peak (GP) can be observed at 319.1 watts with 91.7 volts. The other two local peaks (LP) can be observed at 260.3 watts with 113.5 volts and 255.2 watts with 58.05 volts. The experimental results corresponding to the above PSCs are shown in Fig 3.10 (e)-(h), respectively. It can be observed from Fig. 3.10 (e)-(h) that the GWO-based MPPT algorithm successfully tracks the peak power under all the PSCs, and the steady-state results are oscillation-free and unaffected by the circuitry noise.

Although, the experimental results have been used fixed partial shading conditions only. To simulate the partial shading conditions in the real-world scenario, a combination of simulation tools (like data logger, cloud computing, etc.) controlled shading environments (motorized controlled irradiance, programmable LEDs, etc.), hardware interactive panels (solar simulators) can be adapted for creating a number of dynamic shading patterns. These patterns can be utilized to test the designed topology and to further optimize the constraints of the algorithm to verify the feasibility of the proposed method in practical applications.

3.8 Comparison with the Existing Converters and Latest Methods for PSCs

In Table 3.5, a comparison between the proposed converter and existing converters is presented. It can be observed from Table 3.5 that none of the existing isolated resonant converters has been implemented or tested for the non-uniform irradiance/ partial shading conditions (PSCs) using any optimization/ intelligence-based maximum power point tracking algorithm. Also, for low-power applications, the reliability of the solar-integrated power converter can be improved by using film capacitors for filtering purposes. Further, to the best effort, film capacitors (C_1-C_4) of equal value are selected to avoid the voltage imbalance and maloperation of the proposed converter.

Table 3.5 Comparison of proposed DHABRC with the existing converters

Parameters	[120]	[118]	[121]	[115]	[122]	[119]	[82]	[116]	[117]	**Proposed**
Active switches	8	4	6	4	5	2	2	6	4	4
Diodes	0	0	2	2	6	2	2	2	4	0
Soft-switching	No	Yes	Yes	Yes	Yes	Yes	Yes	Yes	Yes	Yes
Resonance	Yes	Yes	Yes	Yes	Yes	Yes	Partial	Yes	Yes	Yes
Resonating Elements	2	3	3	3	3	3	3	4	3	3
Filtering capacitor	EC	EC	EC	EC+ FC	EC	EC	EC+ FC	EC	EC	FC
PV integration / Algorithm	No	No	No	No	No	No	No	P&O	P&O	GWO
PSCs	No	No	No	No	No	No	No	No	No	Yes

Although many advanced MPPT algorithms, such as MCA-FOCV (a combination of musical chairs algorithm and fractional open-circuit voltage), pigeon-inspired optimization (PIO), and differential evolution (DE), offer fast and highly efficient MPP tracking, these algorithms have not yet been tested for an isolated resonant converter [152], [153], [154].

3.9 Conclusion

The proposed electrolytic capacitor-less dual half-active bridge resonant converter is integrated with Solar PV. A solar PV emulator generates multiple PV curves of different ratings to test the uniform and partially shaded irradiance conditions. The power at global maxima is harnessed using the heuristic approach-based particle swarm optimization and grey wolf optimization MPPT algorithm. Also, due to the direct control approach of these MPPT algorithms, the converter becomes less sensitive to noise and adaptive to dynamic conditions while eliminating the control loop required to generate the phase-shift angle.

Now, since the output voltage of the solar PV integrated proposed converter is still uncontrolled and depends upon the phase-shift angle generated from MPPT algorithm. So, in the next chapter, the proposed electrolytic capacitor-less isolated DC-DC resonant converters will be cascaded with a conventional three-phase voltage source inverter to form a pseudo-DC-link-based two-stage topology, where the topology will be utilized to feed the solar power to the AC grid. For grid integration, synchronous reference frame based PLL is used and control loops are designed are better stability and performance.